HLLC-type methods for compressible two-phase flow in ducts with discontinuous area changes

Alexandra Metallinou Log[a,*], Svend Tollak Munkejord[b], Morten Hammer[b]

[a]*Norwegian University of Science and Technology, Department of Physics, Department of Energy and Process Engineering, NO-7491 Trondheim, Norway*
[b]*SINTEF Energy Research, P.O. Box 4761 Torgarden, NO-7465 Trondheim, Norway*

Abstract

In this work, the Harten-Lax-van Leer Contact (HLLC) approximate Riemann solver is extended to two-phase flow through ducts with discontinuous cross-sections. Two main strategies are explored regarding the treatment of the non-conservative term arising in the governing equations. In the first, labelled HLLC+S, the non-conservative term is discretized separately. In the second, labelled HLLCS, the non-conservative term is incorporated in the Riemann solver. The methods are assessed by numerical tests for single and two-phase flow of CO_2, the latter employing a homogeneous equilibrium model where the thermodynamic properties are calculated using the Peng–Robinson equation of state. The methods have different strengths, but in general, HLLCS is found to work best. In particular, it is demonstrated to be equally accurate and more robust than existing methods for non-resonant flow. It is also well-balanced for subsonic flow in the sense that it conserves steady-state flow.

Keywords: Finite-volume method, HLLC solver, compressible flow, non-conservative system, two-phase flow, variable cross-section, nozzle flow

1. Introduction

The simulation of two-phase flow through ducts with discontinuous cross-sections is essential in several industrial applications. Such simulations are needed for modelling e.g. two-phase flow in wellbores in the oil and gas industry [1], nuclear reactor coolant flows [2], emergency venting of hydrocarbon pipelines [3] and cavitation in refrigeration systems [4]. Systems like those mentioned above can often be modelled

*Corresponding author
Email address: Alexandra.Log@hotmail.com (Alexandra Metallinou Log)

as quasi one-dimensional with discontinuous changes in cross-sectional area of the flow. The system of equations modelling such flow contains a non-conservative term, and this term complicates numerical simulations greatly as it can cause numerical oscillations[5, 6] and divergence [5].

Several authors have constructed numerical methods for the compressible nozzle flow equations [1, 5, 7–9], and systems of similar form [10–16], developing "well-balanced" [17, 18] schemes to capture the flow behaviour at discontinuities. Most of the early research has focused on the special case of single-phase flow with the ideal gas equation of state (EOS). Notable schemes include Kröner and Thanh's well-balanced numerical scheme based on the Lax-Friedrichs flux [19], which was extended for resonant cases in [5], Rochette et al.'s VFRoe based scheme [6] and Cuong et al.'s Godunov scheme based on an exact Riemann solver [8]. Brown et al. [20] proposed the first methodology for resolving two-phase CO_2 flow in pipes with discontinuous cross-sectional area changes for the homogeneous equilibrium two-phase flow model (HEM) with the Peng-Robinson (PR) EOS [21] using the AUSM$^+$-up scheme. Recently, Abbasi et al. [1] developed a Godunov-type scheme for the two-phase drift-flux model with variable cross-section, though with simple EOSs for liquid and gas.

A HLLC-type method has yet to be tested on the problem of compressible flow with discontinuous cross-sections. Note, however, that the HLLC-scheme has been extended for the Euler equations in ducts of *smoothly* varying cross sections [22]. HLLC-type schemes apply information about the eigenstructure of the governing equations in their solution [10, 11, 23], making the schemes less dissipative than general methods such as AUSM$^+$-up [24]. For the application on two-phase flow, the HLLC-scheme's accurate resolution of contact discontinuities [23] is particularly desirable as this also makes the scheme more accurate in resolving transitions between gas, liquid, and mixture flows. As the eigenstructure of the one-dimensional compressible duct flow equations is known, the advantages above motivates the construction of a HLLC solver for this system.

This is further motivated as augmented versions of HLLC have been constructed for similar systems, where abrupt changes are accounted for [10, 11]. An augmented version of HLLC for the Baer-Nunziato (BN) equations [25] was developed by Tokareva and Toro [10], giving promising results for many test cases. The method involves a nonlinear system which was further linearized by Lochon et al. [26]. Murillo and García-Navarro [11] also developed an augmented version of HLLC for the shallow-water equations. This method produced promising results as well, though the authors note difficulties such as the need for a "source-fix" to avoid unphysical solutions in certain cases.

The contribution of this work is to develop and investigate two modified HLLC solvers for compressible duct flow and assess their strengths and weaknesses. In particular, we will consider two-phase flow of CO_2, due to its use as a natural working fluid in refrigeration engineering, and the importance of safe and efficient CO_2 transportation as part of CO_2 capture and storage (CCS) as a climate-change mitigation technology [27]. We show that the present method is both robust and accurate when solving challenging two-phase Riemann problems.

We will first present the equation system in more detail and briefly discuss the Riemann problem for the system in Section 2. The HEM and the PR EOS are outlined in Section 3. The numerical methods are derived in Section 4, the methods are assessed in Section 5, and finally some concluding remarks and suggestions for further work are given in Section 6.

2. Governing equations and the Riemann problem

The system of equations describing compressible one-dimensional flow of a single fluid in a rigid duct of variable cross-sectional area, A, is

$$\boldsymbol{U}_t + \boldsymbol{F}(\boldsymbol{U})_x = \boldsymbol{S}, \tag{1}$$

where

$$\boldsymbol{U} = \begin{pmatrix} \rho A \\ \rho u A \\ E A \\ A \end{pmatrix}, \ \boldsymbol{F}(\boldsymbol{U}) = \begin{pmatrix} \rho u A \\ (\rho u^2 + p) A \\ (E + p) u A \\ 0 \end{pmatrix}, \ \boldsymbol{S} = \begin{pmatrix} 0 \\ p \frac{\partial A}{\partial x} \\ 0 \\ 0 \end{pmatrix}.$$

Here, ρ is the density, u the velocity, $E = \rho(e + \frac{1}{2}u^2)$ the total energy, e the specific internal energy, and p the pressure of the fluid. $\boldsymbol{S}$ is a non-conservative term. The set of equations (1) belongs to the class of non-conservative *resonant* systems [5, 28] meaning that the waves which arise in this system can interact and "resonate" with each other. For smooth solutions, the system (1) can be rewritten in quasi-linear form,

$$\boldsymbol{U}_t + \boldsymbol{A}(\boldsymbol{U})\boldsymbol{U}_x = \boldsymbol{0}, \tag{2}$$

where $\boldsymbol{A}$ is the Jacobian matrix of the system. Note that the non-conservative term has now been moved to the left-hand side of the equation. A full derivation of $\boldsymbol{A}$ for a general EOS can be found in [29, Appendix D], and we have included the full expression of $\boldsymbol{A}$ in Appendix A.

It can be shown [19, 28, 29] that the eigenvalues of $\boldsymbol{A}$ are;

$$\lambda_0 = 0, \quad \lambda_1 = u - c, \quad \lambda_2 = u, \quad \lambda_3 = u + c.$$

Note that any of the eigenvalues λ_1, λ_2, λ_3 may coincide with λ_0, giving rise to resonance in the system [28]. The system of equations is hyperbolic away from the points where $\lambda_1 = \lambda_0$ or $\lambda_3 = \lambda_0$ and nonstrictly hyperbolic when $\lambda_2 = \lambda_0$ [28].

2.1. The Riemann problem

Consider the Riemann problem for compressible duct flow,

$$\boldsymbol{U}_t + \boldsymbol{F}(\boldsymbol{U})_x = \boldsymbol{S}, \tag{3}$$

$$\boldsymbol{U}(x,0) = \begin{cases} \boldsymbol{U}_L, \text{ if } x < 0 \\ \boldsymbol{U}_R, \text{ if } x \geq 0 \end{cases}, \tag{4}$$

where $\boldsymbol{U}_L$ and $\boldsymbol{U}_R$ are two different constant states. A thorough analysis on the characteristic fields, Riemann invariants and the solution to this Riemann problem is presented by Andrianov and Warnecke in [28].

When there is no change in A, $A_L = A_R$, the system (1) reduces to the Euler equations. We then have the same characteristics and Riemann invariants as for the Euler equations associated with the eigenvalues $\lambda_1, \lambda_2, \lambda_3$. The Riemann invariants are

$$s, \; u + \frac{2c}{\Gamma} \;\; \text{across} \;\; \frac{\mathrm{d}x_1}{\mathrm{d}t} = u - c \tag{5}$$

$$u, p \;\; \text{across} \;\; \frac{\mathrm{d}x_2}{\mathrm{d}t} = u \tag{6}$$

$$s, u - \frac{2c}{\Gamma} \;\; \text{across} \;\; \frac{\mathrm{d}x_3}{\mathrm{d}t} = u + c, \tag{7}$$

where s is the specific entropy and Γ is the first Grüneisen parameter,

$$\Gamma = \frac{1}{\rho}\left(\frac{\partial p}{\partial e}\right)_\rho = \frac{1}{\rho c_v}\left(\frac{\partial p}{\partial T}\right)_\rho. \tag{8}$$

Here, c_v is the specific heat capacity at constant volume. Admissible waves for the solution to the Riemann problem are then rarefactions and shocks associated with λ_1, λ_3 and a contact discontinuity associated with λ_2.

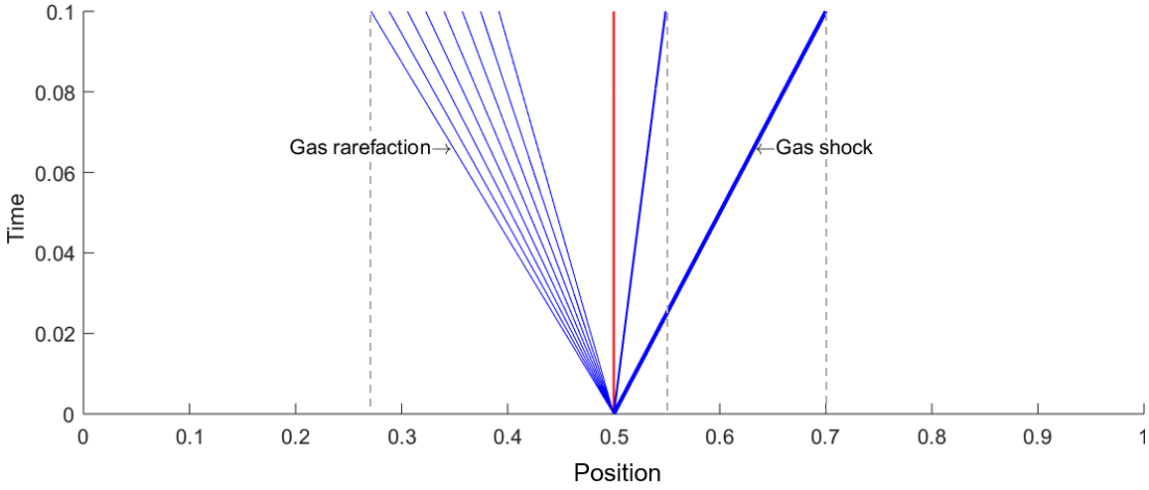

Figure 1: The characteristics of a Riemann problem for 1D compressible duct flow with subsonic flow where $\rho_L > \rho_R$, $p_L > p_R$ and $A_L > A_R$, giving a rarefaction to the left, a stationary contact discontinuity (red), then a contact discontinuity and a shock to the right. Created using [31].

At points with discontinuous area change, there is a a *stationary contact discontinuity* associated with the eigenvalue $\lambda_0 = 0$ [19], the 0-wave. Across the 0-wave we have the following Riemann invariants as shown in [28]

$$A\rho u, \;\; s, \;\; h + \frac{1}{2}u^2, \;\; \text{across} \;\; \frac{\mathrm{d}x_0}{\mathrm{d}t} = \lambda_0 = 0, \tag{9}$$

where $h = e + \frac{p}{\rho}$ is the specific enthalpy of the fluid. The invariants describe the conservation of mass flux, entropy and stagnation enthalpy over the area change. The addition of this wave in the solution to the Riemann problem causes complications such as non-uniqueness [28] and resonance [5, 19, 30]. In Figure 1 we provide an example of the structure of a Riemann problem solution in the case of subsonic flow i.e. $|u| < c$ from left to right. The example was created using Andrianov's program [31] (CONSTRUCT).

3. Thermodynamic models

In this work, we model the fluid as an ideal gas for benchmark tests of numerical solvers of the equation system (1), defined by the equation of state (EOS)

$$p = \rho(\gamma - 1)e, \tag{10}$$

where γ is the ratio of specific heats $\gamma = \frac{c_p}{c_v}$. In addition to benchmark testing, it is also relevant to study the system (1) for two-phase flow of liquid and gas. To model this, we apply the *homogeneous equilibrium model* (HEM) with the Peng-Robinson (PR) EOS [21]. The PR EOS is given by

$$p = \frac{RT}{v_m - b} - \frac{\alpha a}{v_m^2 + 2bv_m - b^2}, \tag{11}$$

where v_m is the specific molar volume of the fluid and R is the gas constant. a, b and α are defined as

$$a = 0.45724 \frac{R^2 T_c^2}{p_c}, \tag{12}$$

$$b = 0.07780 \frac{RT_c}{p_c}, \tag{13}$$

and

$$\alpha = \left[1 + \left(0.37464 + 1.54226\omega - 0.26992\omega^2\right)\left(1 - \sqrt{\frac{T}{T_c}}\right)\right]^2, \tag{14}$$

where T_c, p_c and ω are the critical temperature, critical pressure and the acentric factor of the species. For CO_2, these are

$$p_c = 7.3773\,\text{MPa},\ T_c = 304.35\,\text{K},\ \text{and}\ \omega = 0.2236. \tag{15}$$

The PR EOS only gives residual heat capacities, c_p^{res}, c_v^{res}. In order to compute the total heat capacities $c_p = c_p^{\text{ideal}} + c_p^{\text{res}}, c_v$ in $\text{JK}^{-1}\text{kg}^{-1}$ we use the following estimate,

$$\begin{aligned} c_p^{\text{ideal}} = {} & 479.107 + 1.524318\ T - 1.078176 \cdot 10^{-3}\ T^2 + \\ & + 3.38976 \cdot 10^{-7}\ T^3 + 2.8876 \cdot 10^{-11}\ T^4. \end{aligned} \tag{16}$$

In the HEM it is assumed that the two phases are in thermal, chemical and mechanical equilibrium, which is valid if the phases are well-mixed. Mixture properties are then used in the flow equations (1). In this work, SINTEF's thermodynamic library [32, 33] has been applied to provide solutions for the HEM with the PR EOS. Details on the specific methods applied in the library to obtain relevant variables are presented in [34], though we ignore here the presence of any solid.

4. Numerical methods

The computational domain is discretized in finite volumes Ω_j as depicted in Figure 2. We use two different kinds of finite-volume methods (FVMs) to solve Equation

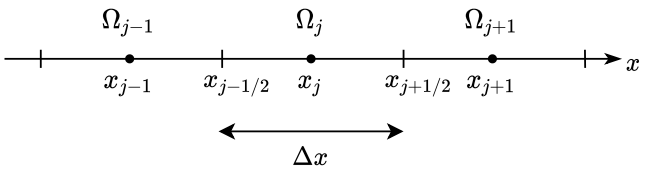

Figure 2: A one dimensional interval subdivided into grid cells, Ω_j, with cell centers at x_j and faces $x_{j-1/2}$, $x_{j+1/2}$.

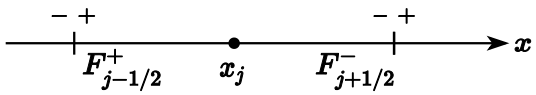

Figure 3: The flux function $\boldsymbol{\mathcal{F}}^+_{j-1/2}$ approximates the flux $\boldsymbol{F}^+_{j-1/2}$ just to the right of the interface at $x_{j-1/2}$. The flux function $\boldsymbol{\mathcal{F}}^-_{j+1/2}$ approximates the flux $\boldsymbol{F}^-_{j+1/2}$ just to the left of the interface at $x_{j+1/2}$.

(1) on this grid. The first FVM is analogous to the spatial discretization that Brown et al. apply in [20], with an Euler time step giving

$$\boldsymbol{U}_j^{n+1} = \boldsymbol{U}_j^n - \frac{\Delta t}{\Delta x}\left(\boldsymbol{\mathcal{F}}_{j+1/2} - \boldsymbol{\mathcal{F}}_{j-1/2}\right) + \Delta t \widetilde{\boldsymbol{S}}_j, \tag{17}$$

where $\boldsymbol{\mathcal{F}} = \boldsymbol{\mathcal{F}}(\boldsymbol{U}_L, \boldsymbol{U}_R)$ is a numerical flux function approximating the average flux $\boldsymbol{F}$ at the cell interfaces $x = x_{j-1/2}, x = x_{j+1/2}$, and $\widetilde{\boldsymbol{S}}_j$ approximates the contribution of the non-conservative term in cell j.

The second FVM is a conservative Godunov scheme which includes the non-conservative term in the numerical flux functions [11]. The FVM takes the following form

$$\boldsymbol{U}_j^{n+1} = \boldsymbol{U}_j^n - \frac{\Delta t}{\Delta x}\left(\boldsymbol{\mathcal{F}}^-_{j+1/2} - \boldsymbol{\mathcal{F}}^+_{j-1/2}\right), \tag{18}$$

where again an Euler time step is used for the temporal discretization. Here, $\boldsymbol{\mathcal{F}}^\pm = \boldsymbol{\mathcal{F}}^\pm(\boldsymbol{U}_L, \boldsymbol{U}_R, \boldsymbol{S})$ are numerical flux functions approximating the average flux, $\boldsymbol{F}$, *right next to* the east, $\boldsymbol{F}^-_{j+1/2}$, and west, $\boldsymbol{F}^+_{j-1/2}$, cell faces as illustrated in Figure 3.

In the following, we will briefly review the HLLC method and then suggest two modified HLLC-type methods to approximate the fluxes for the compressible duct flow.

4.1. The HLLC approximate Riemann solver

The HLLC method, proposed by Toro, Spruce and Speares [23], approximates the cell interface Riemann problem by a three-wave solution;

$$\widetilde{\boldsymbol{U}}(x/t) = \begin{cases} \boldsymbol{U}_L, & \text{if } x < v_L t, \\ \boldsymbol{U}_L^{HLLC}, & \text{if } v_L t \le x < v_C t, \\ \boldsymbol{U}_R^{HLLC}, & \text{if } v_C t \le x < v_R t, \\ \boldsymbol{U}_R, & \text{if } x \ge v_R t, \end{cases} \tag{19}$$

where v_L and v_R are the fastest signal velocities arising from the initial condition of the Riemann problem, and v_C is the speed of the contact wave. The intermediate states $\boldsymbol{U}_L^{HLLC}, \boldsymbol{U}_R^{HLLC}$ are approximated to be constant,

$$\boldsymbol{U}_L^{HLLC} = \frac{1}{\Delta t(v_C - v_L)} \int_{\Delta t v_L}^{\Delta t v_C} \boldsymbol{U}(x, \Delta t)\, \mathrm{d}x \tag{20}$$

and

$$\boldsymbol{U}_R^{HLLC} = \frac{1}{\Delta t(v_R - v_C)} \int_{\Delta t v_C}^{\Delta t v_R} \boldsymbol{U}(x, \Delta t)\, \mathrm{d}x, \tag{21}$$

they are however unknown and must be estimated. HLLC approximates the numerical flux function by

$$\boldsymbol{\mathcal{F}}_{j+1/2} = \begin{cases} \boldsymbol{F}_L, & \text{if } 0 < v_L, \\ \boldsymbol{F}_L^{HLLC}, & \text{if } v_L \le 0 < v_C, \\ \boldsymbol{F}_R^{HLLC}, & \text{if } v_C \le 0 < v_R, \\ \boldsymbol{F}_R, & \text{if } 0 \ge v_R. \end{cases} \tag{22}$$

The intermediate state fluxes, $\boldsymbol{F}_L^{HLLC}$ for positive subsonic flow, and $\boldsymbol{F}_R^{HLLC}$ for negative subsonic flow, are also unknown. In order to determine the fluxes, Rankine-Hugoniot (RH) relations are used across the waves and the additional set of Riemann invariants across the contact discontinuity is applied to close the system. The RH relation states that across a wave

$$\Delta \boldsymbol{F} = v \Delta \boldsymbol{U}, \tag{23}$$

where v is the speed of the wave. For compressible duct flow, we find through some manipulation that the intermediate fluxes $\boldsymbol{F}_K^{HLLC}$, $K = L, R$ can be expressed as

$$\boldsymbol{F}_K^{HLLC} = \boldsymbol{F}_K + v_K(\boldsymbol{U}_K^{HLLC} - \boldsymbol{U}_K), \tag{24}$$

where the intermediate states are approximated by

$$\boldsymbol{U}_K^{HLLC} = \rho_K A_K \left(\frac{v_K - u_K}{v_K - v_C}\right) \begin{pmatrix} 1 \\ v_C \\ \dfrac{E_K}{\rho_K} + (v_C - u_K)\left(v_C + \dfrac{p_K}{\rho_K(v_K - u_K)}\right) \end{pmatrix}, \; K = R, L, \tag{25}$$

and

$$v_C = \frac{p_R - p_L + \rho_L u_L(v_L - u_L) - \rho_R u_R(v_R - u_R)}{\rho_L(v_L - u_L) - \rho_R(v_R - u_R)}. \tag{26}$$

4.2. Wave-speed estimates

The HLLC solver needs estimates for the wave speeds v_L and v_R. There are several different approaches to estimate these wave speeds, some of which are outlined in [35], Section 10.5. In this work, the Roe average wave speed estimate [36] is used. Both Davis [37] and Einfeldt [38] suggest using the Roe averaged eigenvalues for the wave speeds;

$$v_{L,j+1/2} = \min\left(\lambda_1(\boldsymbol{U}_j), \lambda_1(\widehat{\boldsymbol{U}}_{j+1/2})\right), \; v_{R,j+1/2} = \max\left(\lambda_3(\boldsymbol{U}_{j+1}), \lambda_3(\widehat{\boldsymbol{U}}_{j+1/2})\right), \tag{27}$$

where $\widehat{\boldsymbol{U}}$ is the Roe average of the conserved variables. The Roe averaged variables can be found by the Roe averaged matrix $\widehat{\boldsymbol{A}}\left(\boldsymbol{U}_L, \boldsymbol{U}_R\right)$ [36], which must satisfy certain conditions.

We follow the approach of Evje and Flåtten [39] and Munkejord [40] for the two-fluid model, which also involves a non-conservative term, and search for a Roe averaged matrix $\widehat{\boldsymbol{A}}$ which satisfies the following conditions:

R1: $\widehat{\boldsymbol{A}}\left(\boldsymbol{U}_L, \boldsymbol{U}_R\right)(\boldsymbol{U}_R - \boldsymbol{U}_L) = \Delta\boldsymbol{F}(\boldsymbol{U}_L, \boldsymbol{U}_R)$
R2: $\widehat{\boldsymbol{A}}\left(\boldsymbol{U}_L, \boldsymbol{U}_R\right)$ has real eigenvalues and is diagonalizable, and
R3: $\widehat{\boldsymbol{A}}\left(\boldsymbol{U}_L, \boldsymbol{U}_R\right) \rightarrow \boldsymbol{A}(\boldsymbol{U})$ smoothly as $\boldsymbol{U}_L, \boldsymbol{U}_R \rightarrow \boldsymbol{U}$,

wherein $\Delta\boldsymbol{F}(\boldsymbol{U}_L, \boldsymbol{U}_R)$ is formulated as

$$\Delta\boldsymbol{F}(\boldsymbol{U}_L, \boldsymbol{U}_R) = \begin{pmatrix} \{\rho u A\} \\ \{(\rho u^2 + p)A\} - \hat{p}\{A\} \\ \{(E + p)uA\} \\ 0 \end{pmatrix}. \tag{28}$$

Here,

$$\{x\} = x_R - x_L, \tag{29}$$

and $\hat{p}$ is a particular average of the pressures from the left and right states $\hat{p} = \hat{p}(\boldsymbol{U}_L, \boldsymbol{U}_R)$, similarly to $\overline{\alpha}_k(\boldsymbol{U}_L, \boldsymbol{U}_R)$ in [39], [40].

$\widehat{\boldsymbol{A}}$ can be determined by finding a special average of the state vectors $\boldsymbol{U}_L$ and $\boldsymbol{U}_R$, $\widehat{\boldsymbol{U}}(\boldsymbol{U}_L, \boldsymbol{U}_R)$, such that $\widehat{\boldsymbol{A}} = \boldsymbol{A}(\widehat{\boldsymbol{U}})$, $\hat{p} = \hat{p}(\widehat{\boldsymbol{U}})$. A set of averages satisfying R1–R3 are:

$$\widehat{\rho A} = \frac{\rho_L A_L + \rho_R A_R}{2}, \tag{30}$$

$$\hat{A} = \frac{A_L + A_R}{2}, \tag{31}$$

$$\hat{u} = \frac{\sqrt{\rho_L A_L} u_L + \sqrt{\rho_R A_R} u_R}{\sqrt{\rho_L A_L} + \sqrt{\rho_R A_R}}, \tag{32}$$

$$\hat{H} = \frac{\sqrt{\rho_L A_L} H_L + \sqrt{\rho_R A_R} H_R}{\sqrt{\rho_L A_L} + \sqrt{\rho_R A_R}}, \tag{33}$$

where $H_k = h_k + \frac{1}{2}u_k^2$, $k = L, R$.

4.3. HLLC with added non-conservative term, HLLC+S

The HLLC scheme assumes a three wave solution, however we can still apply the scheme to compressible duct flow provided that we also account for the fourth, stationary wave. We apply the FVM (17) with the HLLC numerical flux function. This FVM requires a representation of the non-conservative term, $\widetilde{\boldsymbol{S}}_j$. The discretization of this term requires special care to ensure numerical stability. We follow the approach of Brown et al. [20] for their AUSM$^+$-up scheme and apply a discretization of the non-conservative term which satisfies the non-disturbance relation discussed by Liou et al. [41]. The relation states that under steady conditions with $u = 0$ and $p = \text{const}$.

$$\frac{\partial (Ap)}{\partial x} = p \frac{\partial A}{\partial x}. \tag{34}$$

The following discretization, which satisfies the non-disturbance relation, is used:

$$\widetilde{\boldsymbol{S}}_j = \frac{p_j}{\Delta x} \begin{pmatrix} 0 \\ A_j - A_{j-1} \\ 0 \\ 0 \end{pmatrix}, \text{ if } u_j > 0 \text{ and } \widetilde{\boldsymbol{S}}_j = \frac{p_j}{\Delta x} \begin{pmatrix} 0 \\ A_{j+1} - A_j \\ 0 \\ 0 \end{pmatrix}, \text{if } u_j \leq 0. \tag{35}$$

4.4. HLLCS approximate Riemann solver

We will here derive an augmented version of HLLC, following in part the approach of Murillo and García-Navarro [11] for the shallow-water equations and the approach

of Tokareva and Toro [10] for the Baer-Nunziato equations. We follow the naming convention of Murillo and García-Navarro [11] and call this method "HLLCS", emphasizing that our method is very similar to their discretization of the source term in the shallow-water equations. The HLLCS approximate Riemann solver assumes a four-wave solution instead of a three-wave solution, incorporating the 0-wave. Similarly to HLLC, we will assume that the waves separate constant intermediate states.

For systems in the form of Equation (1), Murillo and García-Navarro derived the following *consistency condition* which the approximate intermediate states must satisfy:

$$\frac{1}{\Delta t(v_R - v_L)} \int_{\Delta t v_L}^{\Delta t v_R} \boldsymbol{U}(x, \Delta t)\, \mathrm{d}x = \frac{v_R \boldsymbol{U}_R - v_L \boldsymbol{U}_L - (\boldsymbol{F}_R - \boldsymbol{F}_L) + \overline{\boldsymbol{S}}}{v_R - v_L}, \tag{36}$$

where

$$\overline{\boldsymbol{S}} = \frac{1}{\Delta t} \int_{x_L}^{x_R} \int_0^{\Delta t} \boldsymbol{S}\, \mathrm{d}t\, \mathrm{d}x. \tag{37}$$

Two different estimates of $\overline{\boldsymbol{S}}$ are used in this work and they are presented in Section 4.4.4. HLLCS will be developed to ensure the subsonic case satisfies the condition (36). For supersonic flow, the fluxes are easily found as will be shown below.

4.4.1. Supersonic flow

For positive supersonic flow, the flux just to the left of the interface, $x = 0$, is simply $\boldsymbol{F}_L$, giving

$$\boldsymbol{\mathcal{F}}^-_{j+1/2} = \boldsymbol{F}_L. \tag{38}$$

The flow just to the right of the interface has passed the area change such that

$$\boldsymbol{\mathcal{F}}^+_{j+1/2} = \boldsymbol{F}_L + \overline{\boldsymbol{S}}. \tag{39}$$

Similarly for negative supersonic flow, the numerical fluxes at Δt become:

$$\boldsymbol{\mathcal{F}}^-_{j+1/2} = \boldsymbol{F}_R - \overline{\boldsymbol{S}}, \tag{40}$$

$$\boldsymbol{\mathcal{F}}^+_{j+1/2} = \boldsymbol{F}_R. \tag{41}$$

4.4.2. Subsonic flow

An illustration of a control volume containing the wave structure of a Riemann problem for positive subsonic flow is shown in Figure 4. In this case there are three unknown intermediate states separated by the stationary wave at $x = 0$ and the contact discontinuity, $\boldsymbol{U}^-_L$, $\boldsymbol{U}^+_R$ and $\boldsymbol{U}^{++}_R$. We approximate the intermediate states,

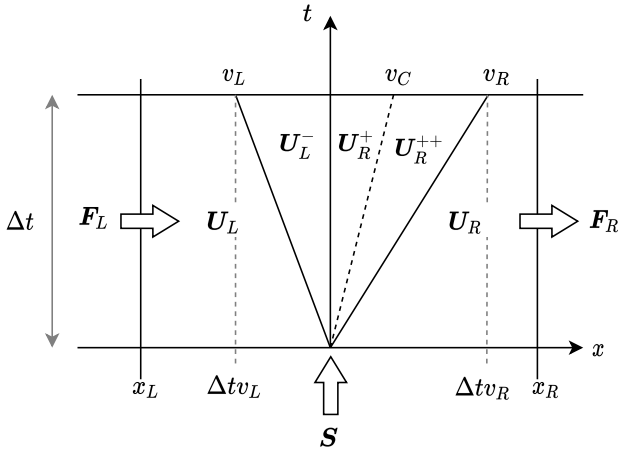

Figure 4: Integration control volume $[x_L, x_R]\times[0, \Delta t]$ in the $x-t$ plane. The control volume contains the two fastest signal velocities, v_L and v_R from the Riemann problem. The solution consists of three inner states separated by the stationary wave at $x = 0$ and the contact discontinuity of positive speed, v_C.

$\boldsymbol{U}_L^-$, $\boldsymbol{U}_R^+$ and $\boldsymbol{U}_R^{++}$ by

$$\left.\begin{aligned} \boldsymbol{U}_L^- &= \frac{1}{-\Delta t v_L}\int_{\Delta t v_L}^{0} \boldsymbol{U}(x,\Delta t)\,\mathrm{d}x \\ \boldsymbol{U}_R^+ &= \frac{1}{\Delta t v_C}\int_{0}^{\Delta t v_C} \boldsymbol{U}(x,\Delta t)\,\mathrm{d}x \\ \boldsymbol{U}_R^{++} &= \frac{1}{\Delta t(v_R - v_C)}\int_{\Delta t v_C}^{\Delta t v_R} \boldsymbol{U}(x,\Delta t)\,\mathrm{d}x \end{aligned}\right\}. \tag{42}$$

In order to estimate the intermediate fluxes, the RH condition is applied across all the waves in the problem. The RH relations are

$$\boldsymbol{F}_L^- - \boldsymbol{F}_L = v_L(\boldsymbol{U}_L^- - \boldsymbol{U}_L), \tag{43}$$

$$\boldsymbol{F}_R^+ - \boldsymbol{F}_L^- - \overline{\boldsymbol{S}} = v(\boldsymbol{U}_R^+ - \boldsymbol{U}_L^-) = \boldsymbol{0}, \tag{44}$$

$$\boldsymbol{F}_R^{++} - \boldsymbol{F}_R^+ = v_C(\boldsymbol{U}_R^{++} - \boldsymbol{U}_R^+), \tag{45}$$

$$\boldsymbol{F}_R - \boldsymbol{F}_R^{++} = v_R(\boldsymbol{U}_R - \boldsymbol{U}_R^{++}). \tag{46}$$

It can be shown that the RH relations (43)-(46) are enough to satisfy the consistency condition (36). To close the system, we impose the Riemann invariants across the

stationary wave and the contact discontinuity,

$$\left.\begin{array}{c} u_R^{++} = u_R^{+} = v_C \\ p_R^{++} = p_R^{+} \end{array}\right\}, \tag{47}$$

$$\left.\begin{array}{c} (A\rho u)_L^{-} = (A\rho u)_R^{+} \\ s_L^{-} = s_R^{+} \\ (\dfrac{u^2}{2} + h)_L^{-} = (\dfrac{u^2}{2} + h)_R^{+} \end{array}\right\}. \tag{48}$$

The RH condition across the wave associated with the wave speed v_L gives

$$\rho_L^{-} = \rho_L \frac{v_L - u_L}{v_L - u_L^{-}}, \tag{49}$$

$$p_L^{-} = p_L + \rho_L (v_L - u_L)(u_L^{-} - u_L), \tag{50}$$

$$E_L^{-} = \rho_L \left(\frac{v_L - u_L}{v_L - u_L^{-}} \right) \left(\frac{E_L}{\rho_L} + (u_L^{-} - u_L) \left(u_L^{-} + \frac{p_L}{\rho_L (v_L - u_L)} \right) \right), \tag{51}$$

and the RH condition across the wave associated with the wave speed v_R gives

$$\rho_R^{++} = \rho_R \frac{v_R - u_R}{v_R - u_R^{++}}, \tag{52}$$

$$p_R^{++} = p_R + \rho_R (v_R - u_R)(u_R^{++} - u_R), \tag{53}$$

$$E_R^{++} = \rho_R \left(\frac{v_R - u_R}{v_R - u_R^{++}} \right) \left(\frac{E_R}{\rho_R} + (u_R^{++} - u_R) \left(u_R^{++} + \frac{p_R}{\rho_R (v_R - u_R)} \right) \right). \tag{54}$$

Equations (49)-(51)and (52)-(54) with the Riemann invariants constitute a nonlinear system which can be solved iteratively. Tokareva and Toro [10] obtained a similar, but larger system of equations which must be solved for the Baer-Nunziato equations.

Both for compressible duct flow and the Baer-Nunziato equations, either the pressures p_L^{-}, $p_R^{+} = p_R^{++}$ or the velocities u_L^{-}, $u_R^{+} = u_R^{++}$ can be chosen as independent variables to solve the system. As stated in [10], there is no difference between the approaches from a theoretical point of view as the two representations of the system are mathematically equivalent. Following Tokareva et al. [10], we choose p_L^{-}, p_R^{+} as the independent variables to ensure pressure positivity when searching for solutions of the system.

We therefore express u_L^- and $u_R^+ = u_R^{++}$ using p_L^- and p_R^+,

$$u_L^-(p_L^-) = u_L + \frac{p_L^- - p_L}{\rho_L(v_L - u_L)}, \tag{55}$$

$$u_R^+(p_R^+) = u_R + \frac{p_R^+ - p_R}{\rho_R(v_R - u_R)}. \tag{56}$$

We then have that $\boldsymbol{U}_L^- = \boldsymbol{U}_L^-(p_L^-)$, such that $s_L^- = s_L^-(p_L^-)$, and enforcing the Riemann invariant $s_L^- = s_R^+ = s$, we have that $s_R^+ = s_R^+(p_L^-)$. The relation for mass flux and the relation for stagnation enthalpy then give the following:

$$\boldsymbol{f} = \begin{pmatrix} A_L\rho_L^-(p_L^-)u_L^-(p_L^-) - A_R\rho_R^+\left(p_R^+, s(p_L^-)\right)u_R^+(p_R^+) \\ h_R^+\left(p_R^+, s(p_L^-)\right) + \frac{1}{2}\left(u_R^+(p_R^+)\right)^2 - \left[h_L^-\left(p_L^-, s(p_L^-)\right) + \frac{1}{2}\left(u_L^-(p_L^-)\right)^2\right] \end{pmatrix} = \boldsymbol{0}. \tag{57}$$

These are two equations for the two independent variables p_L^-, p_R^+. The system (57) can be solved iteratively by e.g. Newton-Raphson's method and it may have zero or up to three solutions. If the system has multiple solutions, we choose the solution which satisfies the following criteria:

C1 The solution is self-consistent in the sense that the Riemann problem for the states $\boldsymbol{U}_L^-(p_L^-), \boldsymbol{U}_R^+(p_L^-, p_R^+)$ provide wavespeed estimates which suggest *subsonic* flow.

C2 The solution has the highest entropy $s_L^-(p_L^-) = s_R^+ = s$ of the self-consistent solutions.

If there are no solutions, we approximate p_L^-, p_R^+ as the point which minimizes the absolute value of $\boldsymbol{f}$.

Once p_L^- and p_R^+ are determined, the state $\boldsymbol{U}_L^-$ can be calculated using Equations (55), (49) and (51). With this we can finally find the unknown fluxes $\boldsymbol{F}_L^-$ and $\boldsymbol{F}_R^+$ from Equation (43) and Equation (44), giving

$$\boldsymbol{F}_L^- = \boldsymbol{F}_L + v_L(\boldsymbol{U}_L^- - \boldsymbol{U}_L), \tag{58}$$

$$\boldsymbol{F}_R^+ = \boldsymbol{F}_L^- + \overline{\boldsymbol{S}}. \tag{59}$$

The negative subsonic flow case can be seen as simply the mirror image of the positive flow case. We now have the states $\boldsymbol{U}_L^{--}$, $\boldsymbol{U}_L^-$ and $\boldsymbol{U}_R^+$ as illustrated in Figure 5. An equivalent system to (57) can be found for this case and the same criteria C1 and C2 can be applied to choose a valid solution.

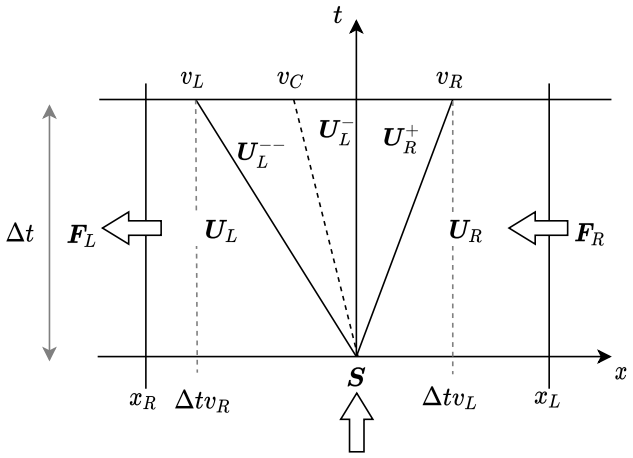

Figure 5: Integration control volume $[x_L, x_R] \times [0, \Delta t]$ in the $x - t$ plane. The control volume contains the two fastest signal velocities v_L, v_R from the Riemann problem. The solution consists of three inner states separated by the stationary wave at $x = 0$ and the contact discontinuity of negative speed, v_C.

4.4.3. Solution for stationary waves

Suppose now that we have the states $\boldsymbol{U}_L$, $\boldsymbol{U}_R$ which satisfy the conditions for a stationary wave across the area change,

$$(A\rho u)_L = (A\rho u)_R, \;\; h_L + \frac{u_L^2}{2} = h_R + \frac{u_R^2}{2}, \;\; s_L = s_R. \tag{60}$$

The exact solution for the Riemann problem (3)–(4) with the two states $\boldsymbol{U}_L$, $\boldsymbol{U}_R$ is a jump from $\boldsymbol{U}_L$ to $\boldsymbol{U}_R$ at the area change. The solution which satisfies the criteria C1 and C2 is $p_L^- = p_L$ and $p_R^+ = p_R$. The intermediate states then become $\boldsymbol{U}_L^- = \boldsymbol{U}_L$ and $\boldsymbol{U}_R^+ = \boldsymbol{U}_R^{++} = \boldsymbol{U}_R$. This means that for stationary waves, when the correct solution is chosen, the intermediate states found in the HLLCS approximate Riemann solver are exact.

4.4.4. The non-conservative term for HLLCS

In this work, two non-conservative terms are tested to estimate the fluxes based on the HLLCS approximate Riemann solver. The first approximate non-conservative term is given by

$$\overline{\boldsymbol{S}}_{\mathrm{RS}} = \begin{pmatrix} 0 \\ \hat{p}\,(A_R - A_L) \\ 0 \\ 0 \end{pmatrix}, \tag{61}$$

where $\hat{p}$ is the Roe-averaged pressure introduced in Section 4.2. We therefore call this the Roe-average-based term (RS). RS is formulated generally such that it may be applied on subsonic, sonic and supersonic flow.

For subsonic flow, the nonlinear system of equations determining the approximate intermediate states and fluxes is solved. The non-conservative term is then given implicitly by the RH conditions. For positive subsonic flow, we get that the non-conservative term must be

$$\overline{\boldsymbol{S}}_{\text{FS+}} = \boldsymbol{F}_R^{++} - v_C(\boldsymbol{U}_R^{++} - \boldsymbol{U}_R^{+}) - \boldsymbol{F}_L^{-}. \tag{62}$$

Similarly for negative subsonic flow, we get that

$$\overline{\boldsymbol{S}}_{\text{FS-}} = \boldsymbol{F}_R^{+} - \boldsymbol{F}_L^{--} + v_C(\boldsymbol{U}_L^{-} - \boldsymbol{U}_L^{--}). \tag{63}$$

As the non-conservative term includes the approximate fluxes, we call it the flux-based term (FS). Note that this estimate only holds if the HLLCS approximate Riemann solver has a solution. FS is only formulated for subsonic flow and may therefore only be applied for subsonic flow problems.

4.4.5. The HLLCS-based fluxes

The HLLCS method approximates the flux functions $\boldsymbol{\mathcal{F}}_{j+1/2}^{-}$ and $\boldsymbol{\mathcal{F}}_{j+1/2}^{+}$ needed for the FVM (18) as shown in Algorithm 1.

Algorithm 1: The HLLCS solver. If subsonic flow is identified, a solver is called to find a valid solution satisfying C1 and C2 or an optimization method is used to minimize $\boldsymbol{f}$. When a solution is found, v_C and the intermediate states $\boldsymbol{U}_L^-$, $\boldsymbol{U}_R^+$ and $\boldsymbol{U}_L^{--}$ or $\boldsymbol{U}_R^{++}$ are returned.

Result: Fluxes for the HLLCS solver, $\boldsymbol{F}_R^+$ and $\boldsymbol{F}_L^-$.
if $v_L > 0$ **then**
  $\boldsymbol{F}_L^- = \boldsymbol{F}_L$
  $\boldsymbol{F}_R^+ = \boldsymbol{F}_L^- + \overline{\boldsymbol{S}}$
end
if $v_L \leq 0$ *and* $v_R > 0$ **then**
  call solver, returning v_C and intermediate states;
  if $v_C \geq 0$ **then**
    $\boldsymbol{F}_L^- = \boldsymbol{F}_L + v_L(\boldsymbol{U}_L^- - \boldsymbol{U}_L)$
    $\boldsymbol{F}_R^+ = \boldsymbol{F}_L^- + \overline{\boldsymbol{S}}$
  else
    $\boldsymbol{F}_R^+ = \boldsymbol{F}_R - v_R(\boldsymbol{U}_R - \boldsymbol{U}_R^+)$
    $\boldsymbol{F}_L^- = \boldsymbol{F}_R^+ - \overline{\boldsymbol{S}}$
  end
end
if $v_R \leq 0$ **then**
  $\boldsymbol{F}_R^+ = \boldsymbol{F}_R$
  $\boldsymbol{F}_L^- = \boldsymbol{F}_R^+ - \overline{\boldsymbol{S}}$
end
Set $\boldsymbol{\mathcal{F}}_{j+1/2}^- = \boldsymbol{F}_L^-$ and $\boldsymbol{\mathcal{F}}_{j+1/2}^+ = \boldsymbol{F}_R^+$.

Remark: Note that for a (subsonic) steady-state wave across the area change, applying $\overline{\boldsymbol{S}}_{\text{FS}}$ will give that $\boldsymbol{\mathcal{F}}_{j+1/2}^- = \boldsymbol{F}_L^- = \boldsymbol{F}_L$ and $\boldsymbol{\mathcal{F}}_{j+1/2}^+ = \boldsymbol{F}_R^+ = \boldsymbol{F}_R$. Inserting this in the FVM (18), we find that

$$\boldsymbol{U}_j^{n+1} = \boldsymbol{U}_j^n \ \forall \ j, \tag{64}$$

i.e. the HLLCS-based FVM with FS conserves the steady-state solution exactly. This means that the FVM is *well-balanced*.

4.5. Summary

In this work, we apply two finite-volume methods HLLC+S and HLLCS. The numerical scheme for the HLLC+S solver is given by

$$\boldsymbol{U}_j^{n+1} = \boldsymbol{U}_j^n - \frac{\Delta t}{\Delta x}\left(\boldsymbol{\mathcal{F}}_{j+1/2} - \boldsymbol{\mathcal{F}}_{j-1/2}\right) + \Delta t \widetilde{\boldsymbol{S}}_j, \tag{65}$$

where the flux functions $\boldsymbol{\mathcal{F}}_{j+1/2}, \boldsymbol{\mathcal{F}}_{j-1/2}$ are given by the HLLC solver, and $\widetilde{\boldsymbol{S}}_j$ is given by Equation (35). The discretization of $\widetilde{\boldsymbol{S}}_j$ is such that the stationary state is conserved.

The HLLCS FVM is given by

$$\boldsymbol{U}_j^{n+1} = \boldsymbol{U}_j^n - \frac{\Delta t}{\Delta x}\left(\boldsymbol{\mathcal{F}}_{j+1/2}^- - \boldsymbol{\mathcal{F}}_{j-1/2}^+\right), \tag{66}$$

where the flux functions $\boldsymbol{\mathcal{F}}_{j+1/2}^-, \boldsymbol{\mathcal{F}}_{j-1/2}^+$ are approximated using the HLLCS approximate Riemann solver as described in Algorithm 1.

5. Assessment of the methods

In this section, we assess the performance of the proposed finite-volume methods, HLLC+S and HLLCS. As the HLLCS FVM is based on a new approximate Riemann solver, we start by testing the HLLCS approximate Riemann solver on local Riemann problems in Section 5.1. We then investigate the performance of the HLLC+S and HLLCS finite-volume methods on benchmark tests for the ideal gas EOS in Section 5.2. The methods are further tested on the HEM with the PR EOS in Section 5.3. We finally compare our methods to the results of different solvers for a water vapour test. Note that for tests with the ideal gas EOS, we use dimensionless variables and denote this by $*/*_{\text{ref}}$, where $*$ is some variable and the subscript ref refers to some reference value.

5.1. Behaviour of the HLLCS approximate Riemann solver for local Riemann problems

As shown in Section 4.4.2 we must solve a nonlinear system, $\boldsymbol{f} = (f_1, f_2)^T = \boldsymbol{0}$, to obtain a solution with the HLLCS approximate Riemann solver for subsonic flow. It is therefore of interest to investigate how this nonlinear system behaves for different local Riemann problems inducing subsonic flow. We investigate this using two modified versions of the common Sod shock-tube problem, giving positive subsonic flow, where we include area change. The values of the left and right states in the Sod shock-tube problem and the left and right areas in the modified tests, Mod. A and Mod. B are given in Table 1.

In Figure 6 we plot for which values of p_L^-, p_R^+ that $f_1 = 0$ and $f_2 = 0$ for the two modified Sod shock-tube tests. When the lines $f_1 = 0$, $f_2 = 0$ cross, $\boldsymbol{f} = \boldsymbol{0}$ has a solution. For Mod. A, there are two possible solutions. We find that the solution to the lower left in Figure 6a is inconsistent as it suggests supersonic flow across the area change even though the Riemann problem is subsonic. The solution to the upper right suggests subsonic flow across the area change and is therefore valid.

Table 1: The left and right states for the Sod shock-tube problem with modified left and right areas for Mod. A and Mod. B.

	p/p_{ref}	u/u_{ref}	ρ/ρ_{ref}	Mod. A: A/A_{ref}	Mod. B: A/A_{ref}
Left	1.0	0.0	1.0	1.0	1.0
Right	0.1	0.0	0.125	0.9	1.1

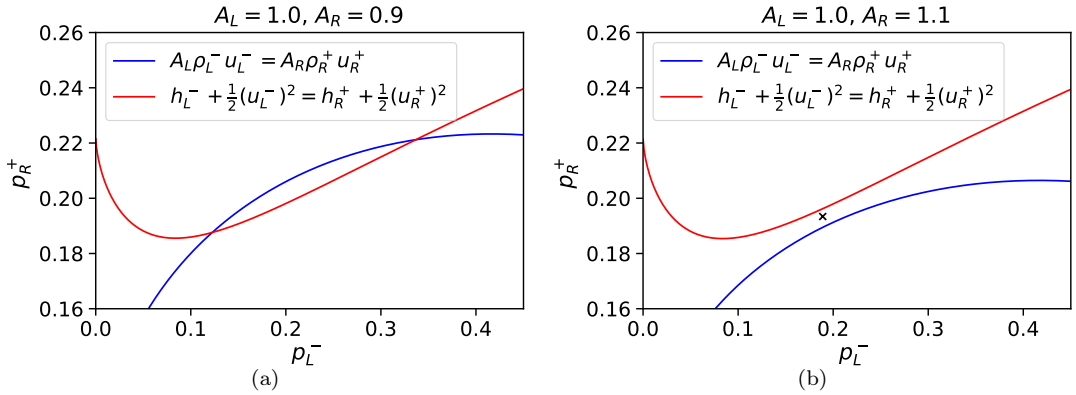

Figure 6: The graphs show for which values of p_L^-, p_R^+ that $f_1 = 0$ (blue) and $f_2 = 0$ (red) for Mod. A (a) and Mod. B (b). For Mod B, an estimate of the point where $|\boldsymbol{f}|$ is minimized is marked with an x.

For Mod. B there is no solution. Mod. B is a resonant case, where a *fifth* wave is induced in the Riemann solution, so the assumption of a four-wave solution in the HLLCS approximate Riemann solver does not hold here. Strictly speaking, the approximate Riemann solver is invalid for resonant cases. We choose the intermediate pressures p_L^-, p_R^+ to estimate the minimum absolute value of $\boldsymbol{f}$, marked with an x in Figure 6b. The resulting intermediate states *approximate* a solution for the HLLCS Riemann solver. These intermediate states do not satisfy the RH relations (43)–(46), however, and the error increases when the area discontinuity or pressure is increased.

5.2. Benchmark tests with the ideal gas EOS

In this section, three selected benchmark tests for compressible duct flow with the ideal gas EOS are used to test the performance of HLLC+S and HLLCS. For all the tests, the CFL number is set to $C = \frac{\max(\lambda)\Delta t}{\Delta x} = 0.9$, extrapolation is used at the boundaries and $\gamma = 1.4$.

Table 2: The left and right states for Test 1.

	p/p_{ref}	u/u_{ref}	ρ/ρ_{ref}	A/A_{ref}
Left	10.0	5.0	0.35	1.0
Right	13.462929846413655	2.695480449295447	0.432823271625514	1.5

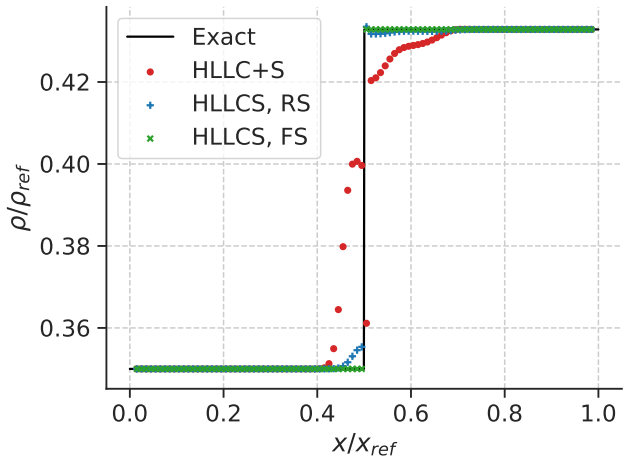

Figure 7: Comparison of the exact density solution (black line) and the solutions of HLLC+S (red circles), HLLCS with RS (blue plus signs) and HLLCS with FS (green crosses) at $t/t_{\text{ref}} = 0.02$ for Test 1.

5.2.1. Test 1: Steady-state

Test 1 is taken from Cuong and Thanh [8], and includes steady flow which satisfies the conditions for a stationary wave across the area change. The initial condition for Test 1 is given in Table 2. For this test, the solution is computed along the interval $x/x_{\text{ref}} \in [0, 1]$, the discontinuity is at $x/x_{\text{ref}} = 0.5$ and $N_{\text{cells}} = 100$. The solutions for HLLC+S and HLLCS at $t/t_{\text{ref}} = 0.02$ are plotted in Figure 7. As expected, HLLCS with FS conserves the steady state because the scheme is well-balanced, as shown in Section 4.4.4. Neither HLLC+S nor HLLCS with RS are well-balanced, however, the solution of HLLCS with RS is not very inaccurate.

We further present a convergence study for HLLC+S and HLLCS with RS for this test. The grids used for the convergence study have tripling numbers of grid cells, N_{cells}, such that cell centres will overlap for all the grids. We calculate the

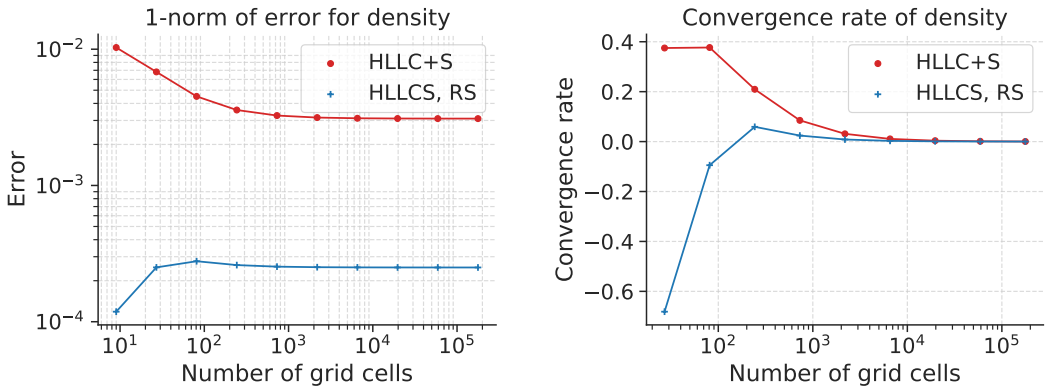

(a) (b)

Figure 8: Results of the convergence test for HLLC+S (red line with circles) and HLLCS with RS (blue line with plus signs) for Test 1.

1-norm of error for the density, the density error, by

$$E_{1,\rho}(\Delta x) = \Delta x \sum_{j=1}^{N_{\text{cells}}} |\rho_j^{\text{exact}} - \rho_j^{\text{approx}}|,$$

where Δx is the grid spacing, and the convergence rate, l, for tripling N_{cells} by

$$l = \frac{1}{\log(3)} \log\left(\frac{E_{1,\rho}(\Delta x)}{E_{1,\rho}(\frac{\Delta x}{3})}\right).$$

The density error for HLLC+S and HLLCS with RS is shown in Figure 8a and the convergence rate for their density solution is shown in Figure 8b. Though HLLCS with RS has a significantly lower error than HLLC+S, both solvers reach a convergence rate of 0. This means that neither of these solvers is consistent.

5.2.2. Test 2: Strong non-conservative term

We now present Test 2, which includes a strong non-conservative term. In Table 3, the initial conditions and intermediate states separating elementary waves of the exact Riemann solution for Test 2 is given. The interval and discontinuity are the same as for Test 1.

The numerical solvers give significant numerical smearing near the area change due to the strong non-conservative term, so a rather fine grid of $N_{\text{cells}} = 1000$ is used to resolve the problem to see clearly how the solvers perform. The density

Table 3: The left and right states for Test 2 including the intermediate states separating elementary waves of the exact Riemann solution for the test ordered from left to right.

	p/p_{ref}	u/u_{ref}	ρ/ρ_{ref}	A/A_{ref}
Left	3.0	-0.90532425	2.191799866	0.9
State 1	1.0	0.1	1.0	0.9
State 2	0.89002806	0.4890494	0.92015244	0.2
State 3	0.89002806	0.4890494	0.5	0.2
Right	0.80290021	0.37372087	0.46454221	0.2

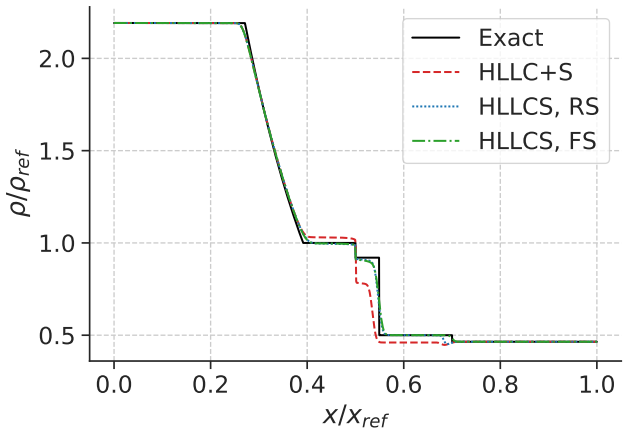

Figure 9: Density solution of HLLC+S (red dashed line), HLLCS with RS (blue dotted line) and HLLCS with FS (green dash-dotted line) compared to the exact solution (black line) for Test 2 at $t/t_{\text{ref}} = 0.1$, with $N_{\text{cells}} = 1000$.

solution for HLLC+S and HLLCS with both RS and FS are compared to the exact solution at $t/t_{\text{ref}} = 0.1$ in Figure 9. The exact solution for the test is produced using CONSTRUCT [31].

For this test, HLLC+S produces unsatisfactory results. The behaviour near the area change does not approximate the exact solution. The density after the area change becomes much too low as compared to the exact solution. Both HLLCS with FS and with RS have numerical smearing between the area change and the contact discontinuity, but appear to approximate the solution well otherwise. HLLCS with RS does not approximate the location of the right shock perfectly, but performs similarly to HLLCS with FS otherwise.

We further present a grid refinement study for this test. The density error for

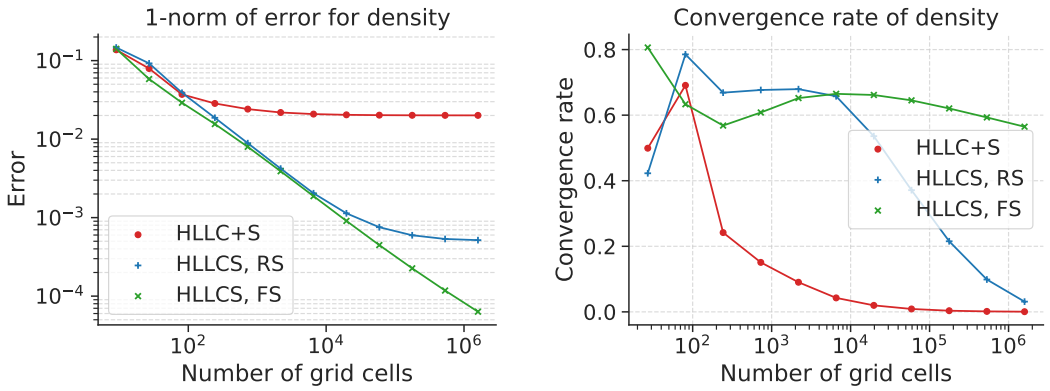

(a) (b)

Figure 10: Results of the convergence test for HLLC+S (red line with circles), HLLCS with RS (blue line with plus signs) and HLLCS with FS (green line with crosses) for Test 2.

the solvers is shown in Figure 10a and the convergence rate for their density solution is shown in Figure 10b. It is clear that HLLCS outperforms HLLC+S. HLLC+S' error settles at approximately 0.02, and its convergence rate goes to 0. HLLCS with RS's convergence rate also goes to zero, though at a much lower density error than HLLC+S. The density error for HLLCS with FS keeps falling for increasing numbers of grid cells and its convergence rate stays above above 0.5 for very fine grids.

5.2.3. Test 3: Resonance

Test 3, suggested by Thanh and Kröner [5], involves the interaction between a rarefaction to the left and an expansion causing the flow to become choked exactly at the area discontinuity. This leads to resonance which induces an "extra" shock in the wave configuration. In Table 4 the initial condition and the states separating elementary waves of the exact Riemann solution are given for Test 3. The solution is computed along the interval $x/x_{\text{ref}} \in [0, 2]$ and the discontinuity is at $x/x_{\text{ref}} = 1$. Following Thanh and Kröner [5], Brown et al. [20], we employ $N_{\text{cells}} = 1000$.

For Test 3, HLLCS with FS fails to compute a solution. The nonlinear system in the HLLCS approximate Riemann solver does not have a solution for the local Riemann problem for this test, similarly to Mod. B in Section 5.1. We compute the intermediate states closest to a solution for the HLLCS Riemann solver. However, as they are not a true solution, the states do not satisfy the RH relations (43)–(46). The FS estimate of the non-conservative term (62) is defined implicitly through these relations and the estimate is poor when inconsistent intermediate states are used in

Table 4: The left and right states for Test 3 and the intermediate states separating elementary waves of the exact Riemann solution ordered from left to right.

	p/p_{ref}	u/u_{ref}	ρ/ρ_{ref}	A/A_{ref}
Left	8.0	0.5	5.0	1.0
State 1	3.5111	1.3306	2.7766	1.0
State 2	1.7227	1.8438	1.6697	1.2
State 3	2.3427	1.5738	2.0779	1.2
State 4	2.3427	1.5738	1.8047	1.2
Right	1.0	0.8	1.0	1.2

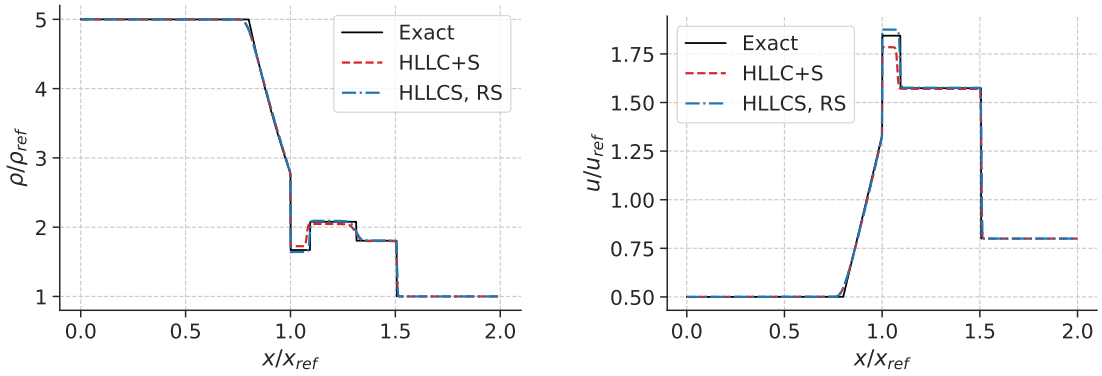

(a) Density

(b) Velocity

Figure 11: Comparison of exact solution (black line) and the density solution (a) and velocity solutions (b) of HLLC+S (red dashed line), and HLLCS with RS (blue dash-dotted line) on Test 3 for velocity at $t/t_{\text{ref}} = 0.2$, $N_{\text{cells}} = 1000$.

its calculation. In this particular case, the error causes HLLCS with FS to obtain negative internal energies during the simulation and crash. HLLCS with RS is less affected by this because the RS discretization does not depend on the intermediate states.

The solutions for density and velocity are given in Figures 11a and 11b respectively for HLLC+S and HLLCS with RS at $t/t_{\text{ref}} = 0.2$ together with points of the exact solution. Both HLLC+S and HLLCS with RS resolve the problem well and there is no sign of instability as often occurs for solvers applied on resonant cases [5]. HLLCS RS approximates the solution better than HLLC+S, which is particularly evident for the density between the stationary wave and the additional shock, for $x/x_{\text{ref}} \in [1, 1.1]$ and between the additional shock and the contact discontinuity,

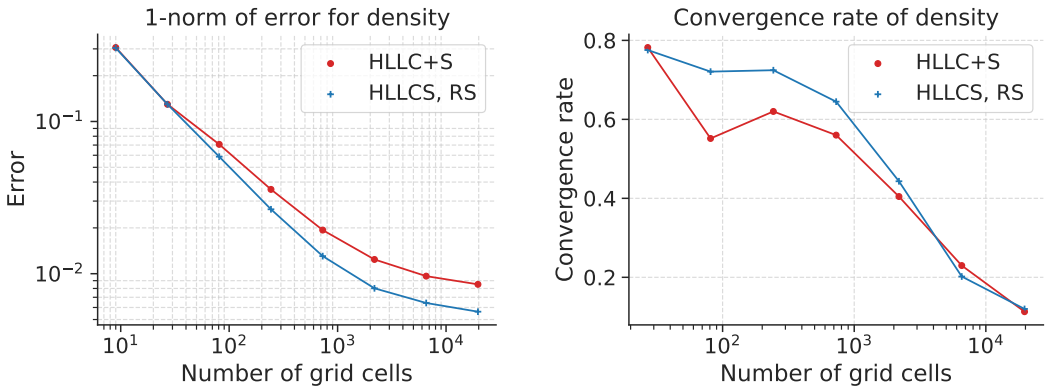

(a) (b)

Figure 12: Results of the convergence test for HLLC+S (red line with circles) and HLLCS with RS (blue line with plus signs) for Test 3.

$x/x_{\text{ref}} \in [1.1, 1.3]$. HLLCS with RS overestimates the velocity of the fluid in the area between the stationary wave and the additional shock. Thanh and Kröner's LxF scheme with the computational corrector does not obtain such an overshoot [5]. Brown et al., however, get a similar overshoot for their AUSM$^+$-up scheme for this test [20]. We present the results of a grid refinement study in Figures 12a and 12b. HLLCS with RS obtains a lower density error than HLLC+S. The convergence rates of both solvers tend to zero, confirming once again that HLLC+S and HLLCS with RS are not consistent for the system.

One should note two things here. Firstly, HLLCS with both FS and RS is *not* generally good at solving resonant problems, but the solver shows promising behaviour and might be modified to work well with resonance. Secondly, even though HLLC+S performed poorly for the stationary state and a strong non-conservative term, it still obtained a reasonable result here. One should not be fooled by this as HLLC+S is generally a poor solver for the system (1).

5.3. Two-phase test with the HEM and the PR EOS

We present here two tests with two-phase CO_2 flow modelled by the HEM with the PR EOS. Test 4 is rather similar to "Test 5" presented by Brown et al. for their AUSM$^+$-up scheme [20]. Our Test 5 includes a stronger non-conservative term than that of Test 4 for which HLLC+S fails to compute a reasonable solution, whereas HLLCS performs well. Note that no exact solution is available for these tests. In order to provide some reference, we compute a solution with our best performing

Table 5: Initial conditions for Test 4.

	p (MPa)	u (ms^{-1})	T (K)	A (m^2)	α_g (-)
Left	5	0	283.547	1	0.0
Right	4	0	278.565	0.5	0.986

solver, HLLCS FS, with a very fine grid on which the discontinuous area change is smoothed over a few grid cells.

5.3.1. Test 4: Two-phase test similar to that of Brown et al.

Test 4 is similar to "Test 5" presented by Brown et al. [20] for the HEM with the PR EOS and a discontinuous cross-sectional area. The initial conditions for Test 4 is given in Table 5, where α_g is the volume fraction of gas. Here, the temperatures and α_g are chosen to match the initial conditions given for "Test 5" in [20], $p_L = 5\,\mathrm{MPa}$, $p_R = 4\,\mathrm{MPa}$, $\rho_L = 829.1\,\mathrm{kg\,m^{-3}}$, $\rho_R = 126.8\,\mathrm{kg\,m^{-3}}$. For the initial state to the right, the volume fraction in [20] is set to $\alpha_R = 0.9$, however our calculations with the PR EOS requires $\alpha_R = 0.986$ to get a density of $126.8\,\mathrm{kg\,m^{-3}}$ at a saturation pressure of 4 MPa for CO_2. We have therefore modified the volume fraction in our initial condition. Furthermore, we choose a CFL number of 0.9 rather than 0.3 as applied by Brown et al. Otherwise, we use the same parameters as Brown et al.: $x \in [0, 1]\mathrm{m}$, the discontinuity is at $x = 0.6\,\mathrm{m}$ and $N_{\mathrm{cells}} = 1000$. For the HLLCS FS reference solution, we apply $N = 9000$ so the area change occurs over 9 grid cells.

The reference solution and the solutions of HLLC+S, HLLCS RS and HLLCS FS for pressure, density, velocity, Mach number, entropy and *mass* fraction of gas are shown in Figures 13a, 13b, 13c, 13d, 13e and 13f, respectively, for $t = 1.2\,\mathrm{ms}$. Similarly to the result in [20], we obtain a rarefaction to the left, a stationary wave at the area change, $x = 0.6\,\mathrm{m}$, a very slow-moving contact discontinuity just to the right of the area change at $x \approx 0.61\,\mathrm{m}$ and a shock to the right. There is an evaporation jump following the shock and further evaporation to the left of the area change as can be seen in the mass fraction of gas in $x \in [0.52, 0.6]\mathrm{m}$, see Figure 13f. This causes a "splitting" of the rarefaction wave as observed in Figure 13a because the wave travels quickly in the pure liquid and more slowly in the two-phase area due to different speeds of sound for single and two-phase flow. The entropy increases at the contact discontinuity. These results are as expected.

We note, however, that HLLC+S's solution contains a spike in the pressure and density at the area change, $x = 0.6\,\mathrm{m}$. Such a spike is not present for the HLLCS solvers. There is no physical reason for a spike to be present in the pressure and density at the area change so this must be caused by the discretization of the non-

Table 6: Initial conditions for Test 5.

	p (MPa)	u (ms^{-1})	T (K)	A (m^2)	α_g (-)
Left	5	0	283.547	1	0.0
Right	3.5	0	280	0.2	0.986

conservative term in HLLC+S. The AUSM$^+$-up scheme presented in [20] also gets a spike in its density solution at the area change. Based on our results, it seems likely that the spike for the AUSM$^+$-up scheme in [20] is also caused by the discretization of the non-conservative term, and that the HLLCS methods are more accurate than the AUSM$^+$-up scheme. HLLCS RS approximates the wavespeeds of the rarefaction and shock less accurately than HLLCS FS and HLLC+S, but seems to perform well otherwise. HLLCS FS appears to be the most accurate, which is reasonable based on the results for the ideal gas tests.

We further present the temperature results for a coarse grid with $N_{\text{cells}} = 100$ and a fine grid with $N_{\text{cells}} = 10000$ in Figures 14a and 14b. HLLCS with FS performs well, even for the coarse grid. HLLCS with RS performs poorly for the coarse grid, but converges towards HLLCS with FS on the fine grid. HLLC+S converges towards an incorrect solution.

5.3.2. Test 5: Two-phase test with a large non-conservative term

We have constructed the present case test to provide a challenging test for the discretization of the non-conservative term. The initial condition is given in Table 6. We employ the same domain, position of the discontinuity, grids and CFL number as in Test 4. We compute a HLLCS FS reference solution on a finer grid for which the area change occurs over 9 grid cells for this test as well.

The reference solution and the solutions of HLLC+S, HLLCS RS and HLLCS FS for pressure, density, velocity, Mach number, entropy and mass fraction of gas are shown in Figures 15a, 15b, 15c, 15d, 15e and 15f, respectively, for $t = 1.2\,\mathrm{ms}$. It is evident in the plots of pressure, density, velocity and Mach number that HLLC+S has failed to compute a reasonable solution and is unstable. In Figure 15a, we have cut off the pressure peak at the area change, $x = 0.6\,\mathrm{m}$ which reaches 14 MPa. Based on the results of this test and further on the result of the steady-state test in Section 5.2.1, we see that imposing the non-disturbance relation [41] for compressible duct flow on the discretization of the non-conservative term is not enough to ensure the stability of the solver. As the discretization of the non-conservative term in the AUSM$^+$-up scheme is only based on this principle, similarly to HLLC+S, the scheme will likely also fail for this test.

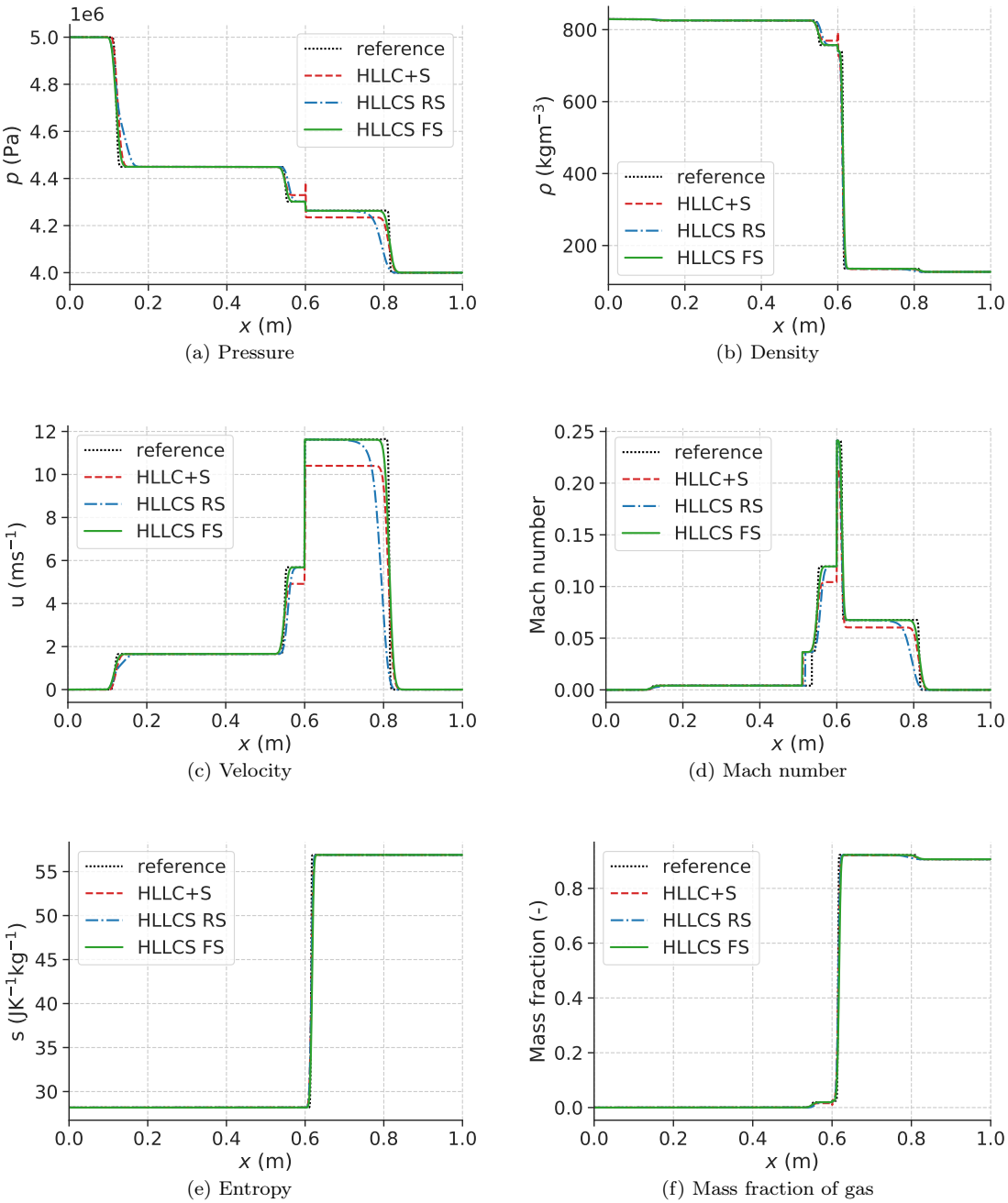

(a) Pressure (b) Density

(c) Velocity (d) Mach number

(e) Entropy (f) Mass fraction of gas

Figure 13: The solutions of HLLC+S (red, dashed line), HLLCS RS (blue, dash-dotted line) and HLLCS FS (green line) for pressure (a), density (b), velocity(c), Mach number (d), entropy (e) and mass fraction of gas (f) for Test 4 at $t = 1.2\,\text{ms}$ with the initial discontinuity at $x = 0.6\,\text{m}$. The result is compared to a reference HLLCS FS solution on a finer grid (black dotted line).

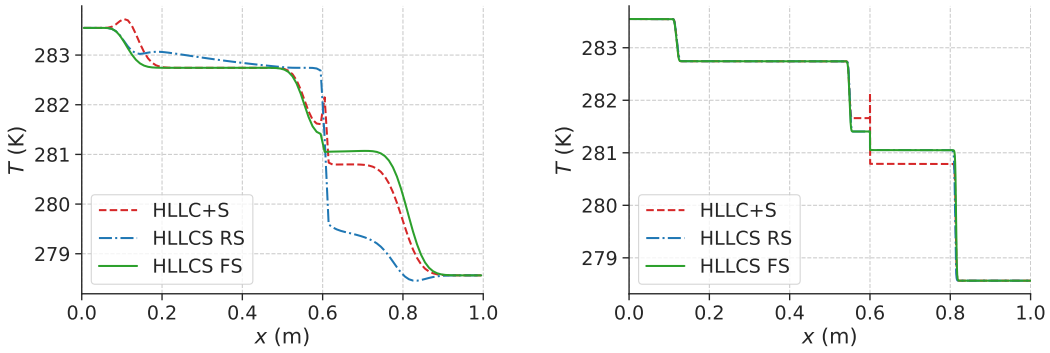

(a) (b)

Figure 14: Temperature results for Test 4 with 100 grid cells (a) and 10000 grid cells (b).

Table 7: Initial conditions for water vapour shock test (Test 6).

	p (MPa)	u (ms^{-1})	T (K)	A (m^2)	α_g (-)
$x \in [0, 2]$	15	0	644.17	0.4	1.0
$x \in [2, 3]$	10	0	607.96	0.4	1.0
$x \in [3, 5]$	10	0	607.96	0.02	1.0

5.4. Test 6: Single-phase steam shock-tube interaction with an abrupt contraction

We will here apply our best performing method, HLLCS with FS, to a water vapour test originally proposed by Tiselj et al. [42] to compare its results with existing methods. In the present work, the IAPWS-95 equation of state is used for modelling water [43], using the TREND software [44]. We compare our results to those of WAHA [42], a HLLC-based method proposed by Daude and Galon [45] and a 2D axisymmetric simulation of the system provided by Daude and Galon [46]. Note that Daude and Galon model the water differently, using steam-water tables based on the 1984 NBS/NRC formulation [47]. The initial conditions for this test is presented in Table 7. The test is run with 2000 grid cells and a CFL number of 0.8. In WAHA, 125 nodes are applied.

The results for pressure and temperature at $t = 2.5\,\text{ms}$ are plotted in Figures 16a and 16b respectively. The schemes perform similarly, except for the calculated plateau between the area change at $x = 3\,\text{m}$ and the transmitted shock wave at $x \approx 3.45\,\text{m}$. The different thermodynamic modelling of water may contribute to the difference in the results, however, as the results agree well for all the other waves in the solution it seems more likely that the difference is related to the numerical

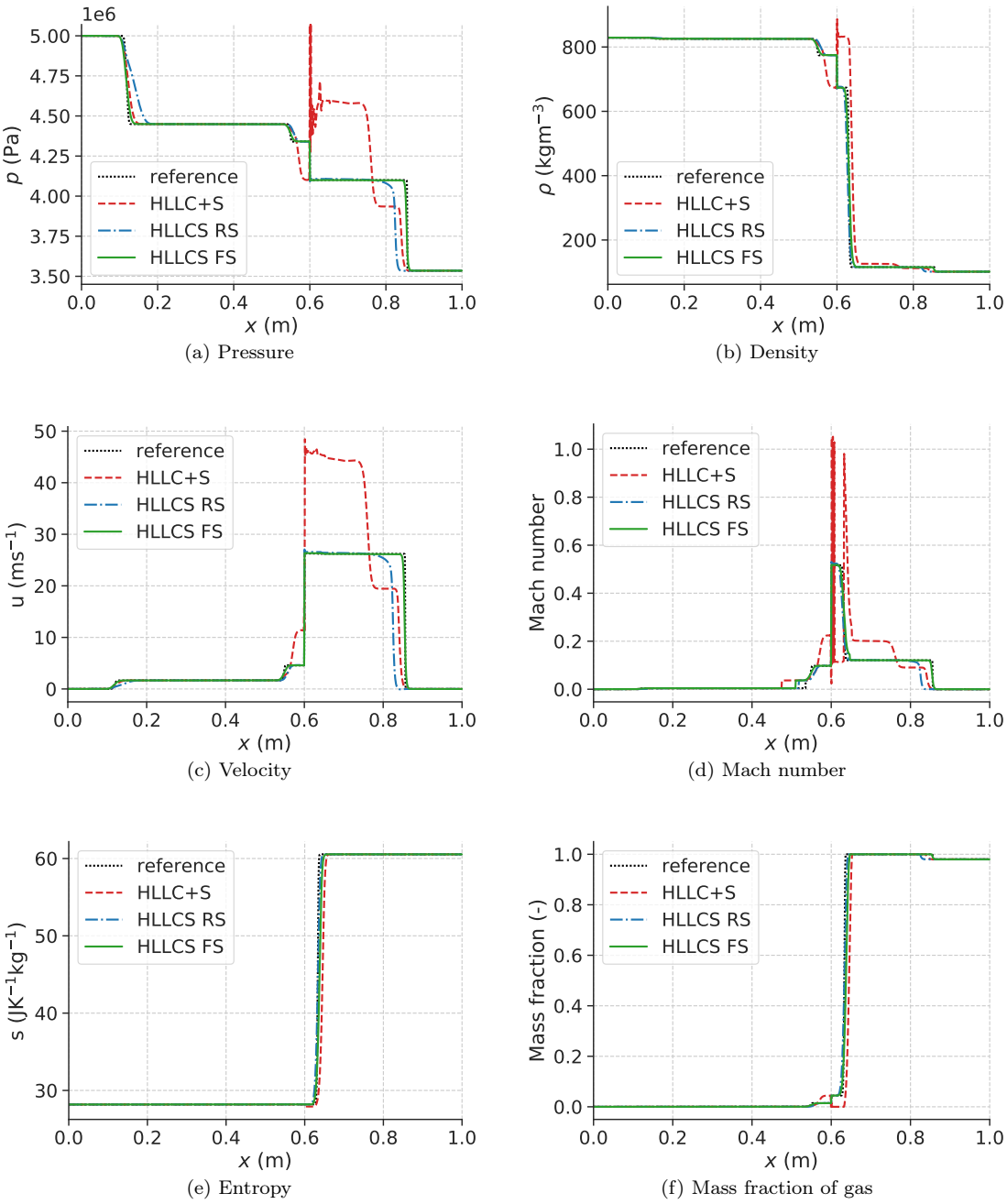

(a) Pressure (b) Density

(c) Velocity (d) Mach number

(e) Entropy (f) Mass fraction of gas

Figure 15: The solutions of HLLC+S (red, dashed line), HLLCS RS (blue, dash-dotted line) and HLLCS FS (green line) for pressure (a), density (b), velocity(c), Mach number (d), entropy (e) and mass fraction of gas (f) for Test 5 at $t = 1.2\,\text{ms}$ with the initial discontinuity at $x = 0.6\,\text{m}$. The result is compared to a reference HLLCS FS solution on a finer grid (black dotted line).

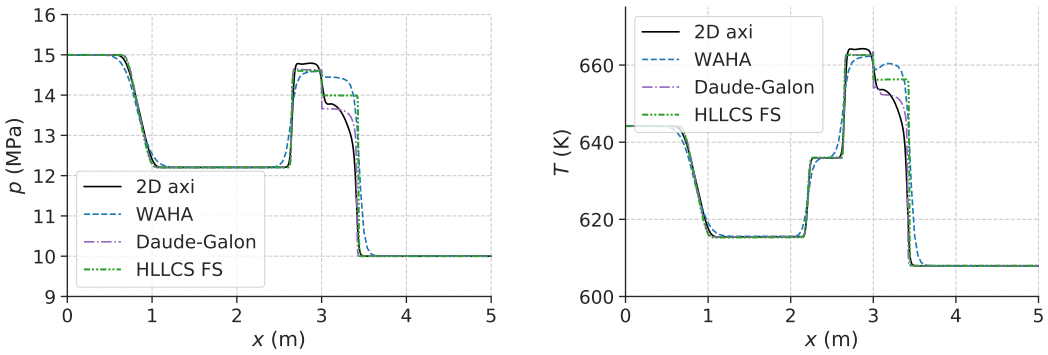

(a) Pressure

(b) Temperature

Figure 16: Test 6: Results of a water vapour shock-tube interaction with an abrupt contraction at $t = 2.5\,\mathrm{ms}$ for HLLCS FS compared with WAHA results from Tiselj et al. [42], the results of Daude and Galon's scheme [45] and a 2D axisymmetric simulation from [46] provided by Daude.

schemes. Daude and Galon's scheme agrees the most with the 2D axisymmetric simulation. However, we note that the 2D result appears to be smeared in this area and the simulation might not be fully converged. Note also that Daude and Galon's scheme obtains a small peak in the temperature at $x = 3.0\,\mathrm{m}$. None of the other solvers obtain this. HLLCS FS is closer to Daude and Galon's scheme and the 2D axisymmetric result than WAHA. The HLLCS FS scheme provides the least smeared result and has no artefacts such as bumps or peaks in its solution. We therefore find the result reasonable.

6. Conclusion

We have proposed HLLC-type finite-volume methods to simulate transient two-phase flow in pipes with discontinuous cross-sectional area. Such simulations are relevant to describe flow in wellbores, nuclear coolant flows and high-pressure pipeline flow.

HLLC+S is a relatively simple scheme, incorporating the non-conservative term in the governing equations much like a source term with a discretization constructed to conserve the stationary state exactly. This approach is similar to that of Brown et al. [20] for an AUSM$^+$-up scheme. HLLCS is a new approximate Riemann solver, assuming a four-wave solution, which includes the non-conservative term in a more thorough manner. For subsonic flow, HLLCS requires the solution of a nonlinear system. Notably, both HLLC+S and HLLCS can be applied with a *general* equation of state.

The methods are tested on benchmark tests with the ideal gas EOS, including a steady-state test, a Riemann problem with a strong non-conservative term and a resonant case. Though HLLC+S performs well for the resonant case, it performs poorly otherwise. This solution scheme is not consistent for the system. We have tested two discretizations of the non-conservative term for the HLLCS-based FVM which we have called FS and RS. FS is based on the flux-estimates of the HLLCS approximate Riemann solver across cell faces, and RS is based on the Roe-average between neighbouring grid cells. It is found that HLLCS does not have a solution for its nonlinear system for resonant flow, where the assumption of a four-wave solution is incorrect. Despite this, HLLCS with RS computes a more accurate solution than HLLC+S for the resonant case. HLLCS with FS does not reach a solution for this case. Otherwise, HLLCS with FS is superior in accuracy and is found to be well-balanced in the sense that it conserves the steady state exactly.

We have further applied the methods to two Riemann problems with two-phase CO_2 flow, governed by a homogeneous equilibrium model (HEM) together with the Peng–Robinson EOS. In the first test we find that HLLC+S has an unphysical behaviour at the area discontinuity. This is not present for the HLLCS solvers. We show with the second test that it is possible to design a case in which HLLC+S diverges whereas HLLCS does not. Finally, we have tested our best performing method, HLLCS with FS, on a test with water vapour and compared our results to other available solvers for the compressible duct flow equations. The result appears reasonable.

Based on these results, HLLCS with FS holds promise as an accurate and robust method to simulate various challenging transient two-phase flow problems. However, HLLCS cannot be applied in cases of flow towards an expansion where the flow becomes choked at the area discontinuity because such cases are resonant. This is a limitation of HLLCS which should be improved upon if the solver is to be used in general industrial applications. Future work includes the extension of HLLCS to resonant flow, possibly by including a fifth wave in its solution, and the derivation of higher-order HLLCS-based methods.

Acknowledgement

This work received support from the NCCS Research Centre, performed under the Norwegian research program Centres for Environment-friendly Energy Research (FME). The authors acknowledge the following partners for their contributions: Aker Carbon Capture, Allton, Ansaldo Energia, Baker Hughes, CoorsTek Membrane Sciences, Equinor, Fortum Varme Oslo, Gassco, Krohne, Larvik Shipping, Lundin Nor-

way, Norcem, Norwegian Oil and Gas, Quad Geometrics, Stratum Reservoir, Total, Vår Energi, Wintershall DEA and the Research Council of Norway (257579).

We are most grateful to Nikolai Andrianov for help with the use of CONSTRUCT, Solomon Brown for a fruitful discussion on Test 4 and Frédéric Daude for providing the results of WAHA, Daude and Galon's solver and the 2D axisymmetric simulation in Test 6. Finally, we would like to thank the reviewers for their detailed feedback which significantly improved the article.

References

[1] M. H. Abbasi, S. N. Lordejani, N. Velmurugan, C. Berg, L. Iapichino, W. H. A. Schilders, N. van de Wouw, A Godunov-type Scheme for the Drift Flux Model with Variable Cross Section, J. Pet. Sci. Eng. 179 (2019) 796 – 813. doi:10.1016/j.petrol.2019.04.089.

[2] R. A. Berry, R. Saurel, O. LeMetayer, The discrete equation method (DEM) for fully compressible, two-phase flows in ducts of spatially varying cross-section, Nucl. Eng. Des. 240 (2010) 3797–3818. doi:10.1016/j.nucengdes.2010.08.003.

[3] R. S. Ettouney, M. A. El-Rifai, A. A. Elzoubier, Emergency venting into redundant pipelines, J. Loss Prev. Process Ind. 25 (2012) 739–745. doi:10.1016/j.jlp.2012.04.009.

[4] J. R. Simões-Moreira, C. W. Bullard, Pressure drop and flashing mechanisms in refrigerant expansion devices, Int. J. Refrig 26 (2003) 840–848. doi:10.1016/S0140-7007(03)00070-7.

[5] M. D. Thanh, D. Kröner, Numerical treatment of nonconservative terms in resonant regime for fluid flows in a nozzle with variable cross-section, Comput. Fluids 66 (2012) 130—-139. doi:10.1016/j.compfluid.2012.06.021.

[6] D. Rochette, S. Clain, T. Buffard, Numerical scheme to complete a compressible gas flow in variable porosity media, Int. J. Comput. Fluid Dyn. 19 (2005) 299–309. doi:10.1080/10618560500162702.

[7] P. Helluy, J. Hérard, H. Mathis, A well-balanced approximate Riemann solver for compressible flows in variable cross-section ducts, J. Comput. and Appl. Mathem. 236 (2012) 1976–1992. doi:10.1016/j.cam.2011.11.008.

[8] D. H. Cuong, M. D. Thanh, Constructing a Godunov-type scheme for the model of a general fluid flow in a nozzle with variable cross-section, Appl. Mathem. and Comput. 305 (2017) 136–160. doi:10.1016/j.amc.2017.01.065.

[9] S. Clain, D. Rochette, First- and second-order finite volume methods for the one-dimensional nonconservative Euler system, J. Comput. Phys. 228 (2009) 8214–8248. doi:10.1016/j.jcp.2009.07.038.

[10] S. A. Tokareva, E. F. Toro, HLLC-type Riemann solver for the Baer–Nunziato equations of compressible two-phase flow, J. Comput. Phys. 229 (2010) 3573–3604. doi:10.1016/j.jcp.2010.01.016.

[11] J. Murillo, P. García-Navarro, Augmented versions of the HLL and HLLC Riemann solvers including source terms in one and two dimensions for shallow flow applications, J. Comput. Phys. 231 (2012) 6861–6906. doi:10.1016/j.jcp.2012.06.031.

[12] T. Gallouët, J. Hérard, N. Seguin, Some approximate Godunov schemes to compute shallow-water equations with topography, Comput. Fluids 32 (2003) 479—-513. doi:10.1016/S0045-7930(02)00011-7.

[13] Q. Liang, F. Marche, Numerical resolution of well-balanced shallow water equations with complex source terms, Adv. Water Resour. 32 (2009) 873—-884. doi:10.1016/j.advwatres.2009.02.010.

[14] E. Audusse, F. Bouchut, M. Bristeau, R. Klein, B. Perthame, A Fast and Stable Well-Balanced Scheme with Hydrostatic Reconstruction for Shallow Water Flows, SIAM J. Sci. Comput. 25 (2006) 2050—-2065. doi:10.1137/S1064827503431090.

[15] D. Rochette, S. Clain, Two-dimensional computation of gas flow in a porous bed characterized by a porosity jump, J. Comput. Phys. 219 (2006) 104–119. doi:10.1016/j.jcp.2006.03.013.

[16] L. Girault, J.-M. Hérard, Multidimensional computations of a two-fluid hyperbolic model in a porous medium, Int. J. Finite Vol. 7 (2010). URL: https://hal.archives-ouvertes.fr/hal-01114209, publisher: Institut de Mathématiques de Marseille, AMU.

[17] F. Bouchut, Nonlinear Stability of Finite Volume Methods for Hyperbolic Conservation Laws and Well-Balanced Schemes for Sources, Birkhäuser, 2004. doi:10.1007/b93802.

[18] J. M. Greenberg, A. Y. Leroux, A Well-Balanced Scheme for the Numerical Processing of Source Terms in Hyperbolic Equations, SIAM J. Numer. Anal. 33 (1996) 1–16. doi:10.1137/0733001, publisher: Society for Industrial and Applied Mathematics.

[19] D. Kröner, M. D. Thanh, Numerical Solutions to Compressible Flows in a Nozzle with Variable Cross-section, SIAM J. Numer. Anal 43 (2005) 796—-824. doi:10.1137/040607460.

[20] S. Brown, S. Martynov, H. Mahgerefteh, Simulation of two-phase flow through ducts with discontinuous cross-section, Comput. Fluids 120 (2015) 46–56. doi:10.1016/j.compfluid.2015.07.018.

[21] D. Y. Peng, D. B. Robinson, A New Two-Constant Equation of State, Ind. Eng. Chem. Fundam. 15 (1976) 59–64. doi:10.1021/i160057a011.

[22] S. LeMartelot, B. Nkong, R. Saurel, Liquid and liquid–gas flows at all speeds, J. Comput. Phys. 255 (2013) 53–82. doi:10.1016/j.jcp.2013.08.001.

[23] E. F. Toro, M. Spruce, W. Speares, Restoration of the contact surface in the HLL-Riemann solver., Shock Waves 4 (1994) 25—-34. doi:10.1007/BF01414629.

[24] O. A. Marzouk, The Sod gasdynamics problem as a tool for benchmarking face flux construction in the finite volume method, Sci. Afr. 10 (2020). doi:10.1016/j.sciaf.2020.e00573.

[25] M. R. Baer, J. W. Nunziato, A two-phase mixture theory for the deflagration-to-detonation transition (ddt) in reactive granular materials, Int. J. Multiphase Flow 12 (1986) 861–889. doi:10.1016/0301-9322(86)90033-9.

[26] H. Lochon, F. Daude, P. Galon, J.-M. Hérard, HLLC-type Riemann solver with approximated two-phase contact for the computation of the Baer–Nunziato two-fluid model, J. Comput. Phys. 326 (2016) 733–762. doi:10.1016/j.jcp.2016.09.015.

[27] S. T. Munkejord, M. Hammer, S. W. Løvseth, CO_2 transport: Data and models - A review, Appl. Energy 169 (2016) 499–523. doi:10.1016/j.apenergy.2016.01.100.

[28] N. Andrianov, G. Warnecke, On the Solution to The Riemann Problem for the Compressible Duct Flow, SIAM J. Appl. Math 64 (2004) 878–901. doi:10.1137/S0036139903424230.

[29] A. M. Log, Development and investigation of HLLC-type finite-volume methods for one and two-phase flow in pipes with varying cross-sectional area, Master's thesis, NTNU, 2020. URL: https://alexandramlog.files.wordpress.com/2020/12/thesis-5-1.pdf.

[30] P. Goatin, P. G. LeFloch, The Riemann problem for a class of resonant hyperbolic systems of balance laws, Annales de l'Institut Henri Poincaré C, Analyse non linéaire 21 (2004) 881–902. doi:10.1016/j.anihpc.2004.02.002.

[31] N. Andrianov, CONSTRUCT, a collection of MATLAB routines for constructing the exact solution to the Riemann problem for the Baer-Nunziato model of two-phase flows, 2004. URL: https://github.com/nikolai-andrianov/CONSTRUCT.

[32] Ø. Wilhelmsen, A. Aasen, G. Skaugen, P. Aursand, A. Austegard, E. Aursand, M. A. Gjennestad, H. Lund, G. Linga, M. Hammer, Thermodynamic modeling with equations of state: Present challenges with established methods, Ind. Eng. Chem. Res. 56 (2017) 3503–3515. doi:10.1021/acs.iecr.7b00317.

[33] SINTEF Energy Research, Thermopack, 2020. URL: https://github.com/sintef/Thermopack.

[34] M. Hammer, Å. Ervik, S. T. Munkejord, Method Using a Density–Energy State Function with a Reference Equation of State for Fluid-Dynamics Simulation of Vapor–Liquid–Solid Carbon Dioxide, Ind. Eng. Chem. Res. 52 (2013) 9965–9978. doi:10.1021/ie303516m.

[35] E. F. Toro, Riemann Solvers and Numerical Methods for Fluid Mechanics - A Practical Introduction, 2nd edition., Springer, Springer Dordrecht Heidelberg London New York, 1999. doi:10.1007/b79761.

[36] P. L. Roe, Approximate Riemann Solvers, Parameter Vectors, and Difference Schemes., J. Comput. Phys. 43 (1981) 357–372. doi:10.1016/0021-9991(81)90128-5.

[37] S. F. Davis, Simplified Second-Order Godunov-Type Methods., SIAM J. Sci. Stat. Comput. 9 (1988) 445–437. doi:10.1137/0909030.

[38] B. Einfeldt, On Godunov-type methods for gas dynamics., SIAM J. Numer. Anal. 25 (1988) 294—-318. doi:10.1137/0725021.

[39] S. Evje, T. Flåtten, Hybrid flux-splitting schemes for a common two-fluid model, J. Comput. Phys. 192 (2003) 175–210. doi:10.1016/j.jcp.2003.07.001.

[40] S. T. Munkejord, Comparison of Roe-type methods for solving the two-fluid model with and without pressure relaxation, Comput. Fluids 36 (2007) 1061–1080. doi:10.1016/j.compfluid.2007.01.001.

[41] M. Liou, C. Chang, L. Nguyen, T. G. Theofanous, How to Solve Compressible Multifluid Equations: A Simple, Robust, and Accurate Method, AIAA J. 46 (2008) 2345—-2356. doi:10.2514/1.34793.

[42] I. Tiselj, A. Horvat, G. Cerne, J. G. J., I. Parzer, B. Mavko, M. Giot, J. M. Seynhaeve, B. Kucienska, H. Lemonnier, WAHA3 code manual, Final report of the WAHALoads project, Technical Report, FIKS-CT-2000-00106, EU 6th program, 2004.

[43] W. Wagner, A. Pruß, The IAPWS Formulation 1995 for the Thermodynamic Properties of Ordinary Water Substance for General and Scientific Use, J. Phys. Chem. Ref. Data 31 (2002) 387–535. doi:10.1063/1.1461829, publisher: American Institute of Physics.

[44] R. Span, T. Eckermann, S. Herrig, S. Hielscher, A. Jäger, M. Thol, TREND. Thermodynamic reference and engineering data 3.0, 2016. Lehrstuhl für Thermodynamik, Ruhr-Universität Bochum.

[45] F. Daude, P. Galon, A Finite-Volume approach for compressible single- and two-phase flows in flexible pipelines with fluid-structure interaction, J. Comput. Phys. 362 (2018) 375–408. doi:10.1016/j.jcp.2018.01.055.

[46] F. Daude, P. Galon, Simulations of single- and two-phase shock tubes across abrupt changes of area and branched junctions, Nucl. Eng. Des. 365 (2020). doi:10.1016/j.nucengdes.2020.110734.

[47] L. Haar, J. S. Gallangher, G. Kell, NBS/NRC Steam Tables: Thermodynamic and Transport Properties and Computer Programs for Vapor and Liquid States of Water in SI Units., Hemisphere Publishing Co., 1984.

Appendix A. Jacobian matrix of compressible duct flow

For smooth solutions, the compressible duct flow equations can be expressed as

$$\boldsymbol{U}_t + \boldsymbol{A}(\boldsymbol{U})\boldsymbol{U}_x = \boldsymbol{0}, \tag{A.1}$$

where $\boldsymbol{A}$ is the Jacobian matrix of the system. If the pressure is given by some general equation of state (EOS), $p = p(e, \rho)$ a small change in pressure, $\mathrm{d}p$, can be expressed as

$$\mathrm{d}p = \left(\frac{\partial p}{\partial \rho}\right)_e \mathrm{d}\rho + \left(\frac{\partial p}{\partial e}\right)_\rho \mathrm{d}e = (c^2 - \Gamma\frac{p}{\rho})\,\mathrm{d}\rho + \Gamma\rho\,\mathrm{d}e, \tag{A.2}$$

where c is the speed of sound and Γ is the first Grüneisen parameter. Then $\boldsymbol{A}(\boldsymbol{U})$ is given by Equation (A.3).

$$\boldsymbol{A} = \begin{pmatrix} 0 & 1 & 0 & 0 \\ c^2 - u^2 - \Gamma(e + \frac{p}{\rho} - \frac{1}{2}u^2) & (2-\Gamma)u & \Gamma & p\Gamma - \rho c^2 \\ u\left(c^2 - (\Gamma+1)(e + \frac{1}{2}u^2 + \frac{p}{\rho}) + \Gamma u^2\right) & e + \frac{p}{\rho} + \frac{1}{2}u^2 - \Gamma u^2 & (\Gamma+1)u & u\left(p(\Gamma+1) - \rho c^2\right) \\ 0 & 0 & 0 & 0 \end{pmatrix} \tag{A.3}$$